DOI: 10.1002/ ((please add manuscript number))
Article type: Full Paper

Au-manganese oxide nanostructures by a plasma-assisted process as electrocatalysts for oxygen evolution: a chemico-physical investigation

Lorenzo Bigiani, Alberto Gasparotto, Teresa Andreu, Johan Verbeeck, Cinzia Sada, Evgeny Modin, Oleg I. Lebedev, Juan Ramón Morante, Davide Barreca,* and Chiara Maccato*

[*] Dr. L. Bigiani, Prof. A. Gasparotto, Prof. C. Maccato
Department of Chemical Sciences, Padova University and INSTM, 35131 Padova, Italy
E-mail: alberto.gasparotto@unipd.it

Dr. T. Andreu, Prof. J. R. Morante
Catalonia Institute for Energy Research - IREC, Sant Adrià de Besòs, 08930 Barcelona, Spain
Universitat de Barcelona (UB), 08028 Barcelona, Spain

Prof. Johan Verbeeck
EMAT and NANOlab Center of Excellence, University of Antwerp, 2020 Antwerpen, Belgium

Prof. C. Sada
Department of Physics and Astronomy, Padova University and INSTM, 35131 Padova, Italy

Dr. Evgeny Modin
CIC nanoGUNE BRTA, 20018 Donostia - San Sebastian, Spain

Dr. Oleg I. Lebedev
Laboratoire CRISMAT, UMR 6508 CNRS/ENSICAEN/UCBN, 14050 Caen Cedex 4, France

[*] Dr. D. Barreca
CNR-ICMATE and INSTM, Department of Chemical Sciences, Padova University, 35131 Padova, Italy
E-mail: davide.barreca@unipd.it

Keywords: manganese oxides; strong metal–support interaction; plasma assisted-chemical vapor deposition; sputtering; oxygen evolution reaction

Abstract: Earth-abundant and eco-friendly manganese oxides are promising platforms for the oxygen evolution reaction (OER) in water electrolysis. Herein, we report on a versatile and potentially scalable route to gold-decorated manganese oxide-based OER electrocatalysts. In particular, Mn_xO_y (MnO_2, Mn_2O_3) *host* matrices are grown on conductive glasses by plasma

assisted-chemical vapor deposition (PA-CVD), and subsequently functionalized with gold nanoparticles (*guest*) as OER activators by radio frequency (RF)-sputtering. The final selective obtainment of MnO_2- or Mn_2O_3-based systems is then enabled by annealing under oxidizing or inert atmosphere, respectively. A detailed material characterization evidences the formation of high-purity Mn_xO_y dendritic nanostructures with an open morphology and an efficient *guest* dispersion into the *host* matrices. The tailoring of Mn_xO_y phase composition and *host-guest* interactions has a remarkable influence on OER activity yielding, for the best performing Au/Mn_2O_3 system, a current density of ≈5 mA/cm^2 at 1.65 V *vs*. the reversible hydrogen electrode (RHE) and an overpotential close to 300 mV at 1 mA/cm^2. Such results, comparing favorably with literature data on manganese oxide-based materials, highlight the importance of compositional control, as well as of surface and interface engineering, to develop low-cost and efficient anode nanocatalysts for water splitting applications.

1. Introduction

The design and development of cost-effective, durable and highly active electrode materials for the oxygen evolution reaction (OER) is a critical issue towards commercially viable solutions for electrochemical water splitting, CO_2 reduction, regenerative low-temperature fuel cells, and rechargeable metal-air batteries.[1-6] In particular, the first kind of process has received a considerable attention for the hydrogen generation, a strategically attractive energy vector, from water, an abundant natural resource, with no release of toxic/harmful byproducts and in full compliance with the most stringent environmental requirements.[7-13] Nevertheless, OER imposes a large overpotential due its inherently sluggish kinetics, related, in turn, to the energy demanding multiple bond rearrangements and the associated complex multi-electron transfer steps.[4,8,12,14-17] Up to date, few catalysts have provided OER electrocatalytic activities and low overpotentials viable for practical applications, and most of them are based on metals/metal oxides containing rare, expensive and toxic elements, such as Ru and Ir.[2,7,9,10,17-19] As a

consequence, there is an open demand for novel non-noble metal oxides combining optimal catalytic performances with low cost and high durability.[3,8,13,14,20]

Among the possible alternatives, manganese oxides (Mn_xO_y) and, in particular, MnO_2 and Mn_2O_3, come to the fore thanks to their low toxicity, large natural abundance, and rich redox chemistry.[4,5,8,9,12,18,19,21-23] So far, Mn_xO_y-based OER catalysts have demonstrated a good structural stability and encouraging performances in alkaline media,[1-3,6,11] although the exact role of Mn_xO_y phase composition, as well as of surface and defect chemistry, undoubtedly require further investigation.[4,9,13,18,23,24]

So far, various strategies have been proposed and applied to tailor Mn_xO_y-based material chemico-physical properties and functional performances for the target applications.[7,9,21,25] In this regard, an amenable approach involves the controlled fabrication of multi-component systems, which offer additional degrees of freedom with respect to their single phase counterparts.[1,3,14,17,22] In this scenario, functionalization with Au nanoparticles (NPs) even in trace amounts has proved to be effective in enhancing oxygen evolution performances, due to local interactions at Au/Mn_xO_y neighboring sites.[1,2,8] In particular, the occurrence of a strong metal-support interaction (SMSI) at the Au/Mn_xO_y interface involves a charge redistribution between *guest* metal and *host* support.[2,21,26,27] This phenomenon, in turn, involves the formation of oxygen vacancies on manganese oxide at the interface with Au NPs.[28-31] Overall, the control of the aforementioned effects through a controllable material design and processing is of outstanding importance to achieve enhanced OER performances.

In the present study, Mn_xO_y (MnO_2, Mn_2O_3) nanomaterials (*host*) are grown on fluorine-doped tin oxide (FTO) substrates by plasma assisted-chemical vapor deposition (PA-CVD), functionalized with gold NPs (*guest*) by radio frequency (RF)-sputtering under mild conditions, and subjected to *ex-situ* thermal treatment (Scheme 1). The advantages of the proposed synthetic approach are: i) the direct obtainment of supported, mechanically stable materials, avoiding typical drawbacks of the homologous powdered ones (*e.g.* the need for post-synthesis

immobilization procedures);[5,9,11,23,32] ii) the possibility of selectively directing the *host* matrix evolution to Mn(IV) or Mn(III) oxide starting from the same manganese oxide deposits, as a function of the annealing atmosphere (air or Ar, respectively);[18,25] iii) the obtainment of a tailored Au NP dispersion, as well as of an intimate *host-guest* contact;[33,34] iv) the introduction of oxygen vacancies during the PA-CVD, RF-sputtering and annealing steps.[25,29,35]

The advantages offered by the adopted preparation route provide a versatile toolkit for the mastering of material characteristics. In this work, interrelations between preparative conditions and the chemico-physical properties and OER functional behavior of the developed Mn_xO_y-based materials are presented and critically discussed, proposing also a possible mechanism accounting for the improved performances achieved upon gold functionalization.

2. Results and Discussion

MnO_2- and Mn_2O_3-based samples were grown on FTO-coated glass supports according to the synthetic approach shown in Scheme 1 (see Experimental Section for further details).

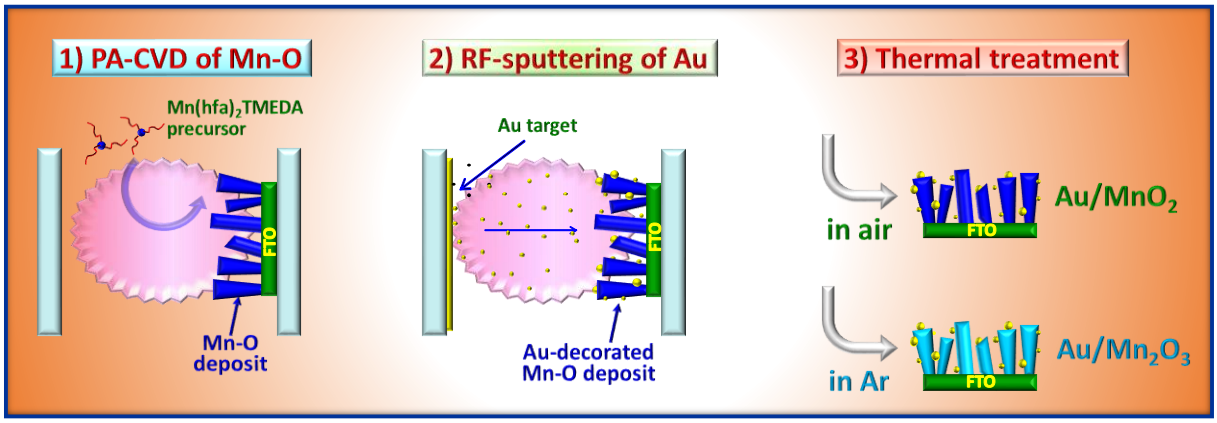

Scheme 1. Sketch of the procedure adopted for the preparation of Au/MnO_2 and Au/Mn_2O_3 samples. For comparison purposes, bare Mn_xO_y (MnO_2, Mn_2O_3) systems were also synthesized by PA-CVD (step 1) and final thermal treatment either in air or Ar (step 3).

For air-annealed samples, X-ray diffraction (XRD) analyses (Figure 1a) revealed, besides FTO substrate reflections, two signals at $2\theta = 28.7°$ and 37.3°, that could be indexed to the (110) and (101) crystalline planes of β-MnO_2 (*pyrolusite*)[34,36,37] (mean crystallite size ≈20 nm). In a

different way, for specimens subjected to thermal treatment under Ar, the diffraction peaks at $2\theta = 23.2°$, 33.1° and 38.3° well matched with the (211), (222) and (400) reflections of β-Mn_2O_3 (*bixbyite*)[15,38] (average crystallite dimensions ≈45 nm). The relatively weak and broad Mn_xO_y (MnO_2, Mn_2O_3) signals indicated a high material defectivity,[32,34] as further discussed below. The absence of reflections from metallic Au was traced back to the relatively low content and high dispersion of gold particles.[2,33]

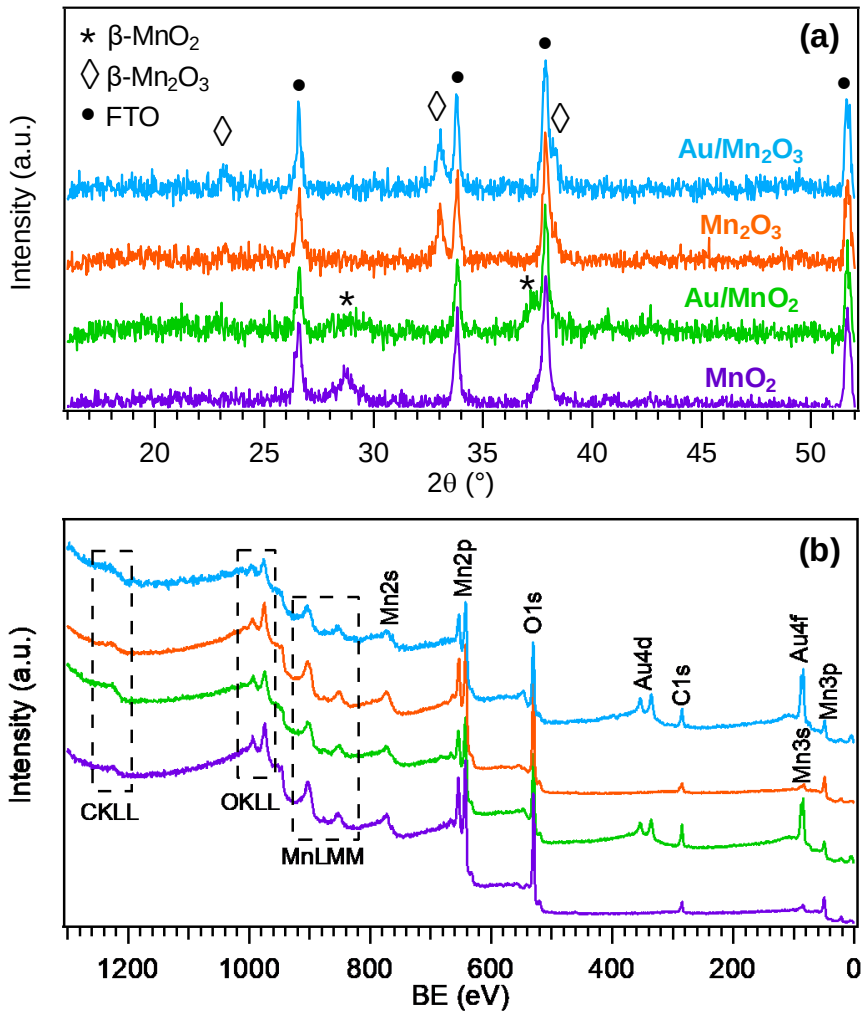

Figure 1. XRD patterns (a) and XPS survey spectra (b) of bare and gold-decorated Mn_xO_y (MnO_2, Mn_2O_3) samples.

X-ray photoelectron spectroscopy (XPS) analyses were run to investigate the surface composition of the synthesized materials. As can be observed from Figure 1b, the main Au photoelectron peaks could be clearly discerned in the wide-scan spectra of gold-decorated

samples. Nonetheless, such specimens clearly revealed the manganese and oxygen signals detected also on the corresponding gold-free samples. Taking into account the surface sensitivity of the XPS techniques, these results suggest an effective dispersion of Au nanoparticles on Mn_xO_y (MnO_2, Mn_2O_3) and the formation of a high density of Au/Mn_xO_y junctions, a favorable issue in view of electrocatalytic applications.[33,39]

In agreement with the above XRD results, the high resolution Mn2p and Mn3s XPS signals (Figure 2a and 2b, respectively) confirmed the obtainment of pure MnO_2- and Mn_2O_3-based materials for both bare and gold-decorated Mn_xO_y systems. In fact, for air-annealed samples, the Mn2p XPS spectrum showed two spin-orbit components at binding energies (BE) of 642.5 and 654.1 eV corresponding to $Mn2p_{3/2}$ and $Mn2p_{1/2}$, respectively, in line with literature data for manganese(IV) oxide.[32,37,40,41] This conclusion was further confirmed by the BE difference between the $Mn2p_{3/2}$ peak and the O1s lattice component (**I**, see below) of 112.7 eV,[33,34] as well as by the Mn3s multiplet splitting separation of 4.7 eV.[10,37,39] As far as specimens annealed in Ar are concerned, the $Mn2p_{3/2}$ and $Mn2p_{1/2}$ component BEs shifted to 641.8 and 653.5 eV.[11,16] In addition, the $Mn2p_{3/2}$-O1s BE difference and the Mn3s multiplet splitting separation were 111.6 eV and 5.3 eV, respectively. As a whole, these results support the obtainment of manganese(III) oxide.[15,16,19,41]

For all samples, two components contributed to the O1s signal (Figure 2c). The main one, located at BE = 529.8-530.1 eV (**I**), was ascribed to Mn-O-Mn bonds, whereas a second one at 531.6-532.0 eV (**II**) was attributed to -OH groups chemisorbed on oxygen vacancies.[32,34,35,37,40,42] Interestingly, the contribution of the latter component to the whole O1s signal increased of ≈10 % on going from bare Mn_xO_y (MnO_2, Mn_2O_3) systems to the corresponding gold-decorated ones, indicating a higher concentration of oxygen defects on Au/MnO_2 and Au/Mn_2O_3 specimens. This phenomenon likely arises from two concomitant effects taking place during the sputtering step (see Scheme 1): i) the bombardment of Mn_xO_y surface by Ar^+ species;[29,35] ii) the occurrence of a SMSI effect at the Au/Mn_xO_y interface (see

below for further details), involving the formation of additional oxygen vacancies following a *host-guest* charge redistribution.[26,28-31]

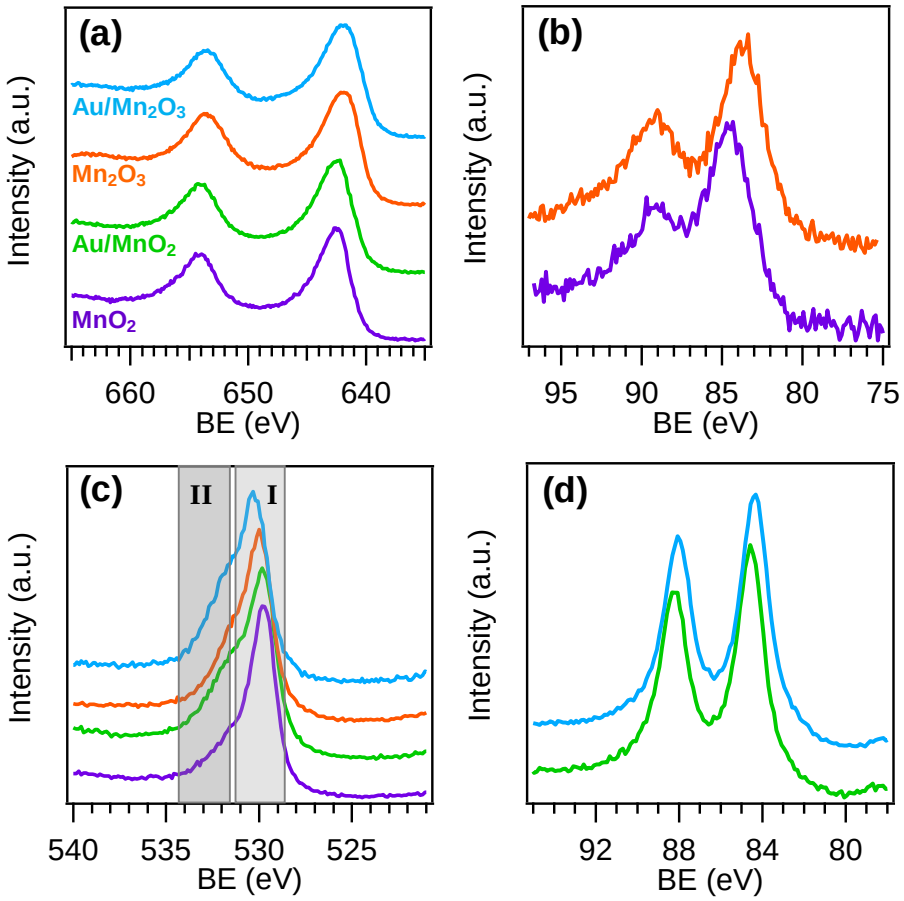

Figure 2. Surface Mn2p (a), Mn3s (b), O1s (c) and Au4f (d) XPS signals for bare and gold-decorated Mn_xO_y (MnO_2, Mn_2O_3) samples. Color codes as in panel (a).

The $Au4f_{7/2}$ and $Au4f_{5/2}$ spin orbit components (Figure 2d) were located at 84.5 and 88.1 eV, respectively. Such values, ≈0.5 eV higher that those typically reported for Au(0),[41] suggested an appreciable electron transfer from gold NPs to Mn_xO_y at the metal/oxide interface, in line with the above mentioned SMSI effect.[28-31,39,43] This phenomenon, reasonably enhanced by the efficient dispersion of gold nanoparticles even in the voids between Mn_xO_y nanostructures (see below), is expected to play a beneficial influence on the OER electrocatalytic behavior of the developed nanocomposites.[28,31,43] Quantitative analyses (see also Supporting Information, § S.1 and Figure S1) yielded an Au/Mn atomic ratio of ≈0.20 for both Au/MnO_2 and Au/Mn_2O_3

specimens, indicating a comparable surface coverage of the *host* matrices by Au NPs.

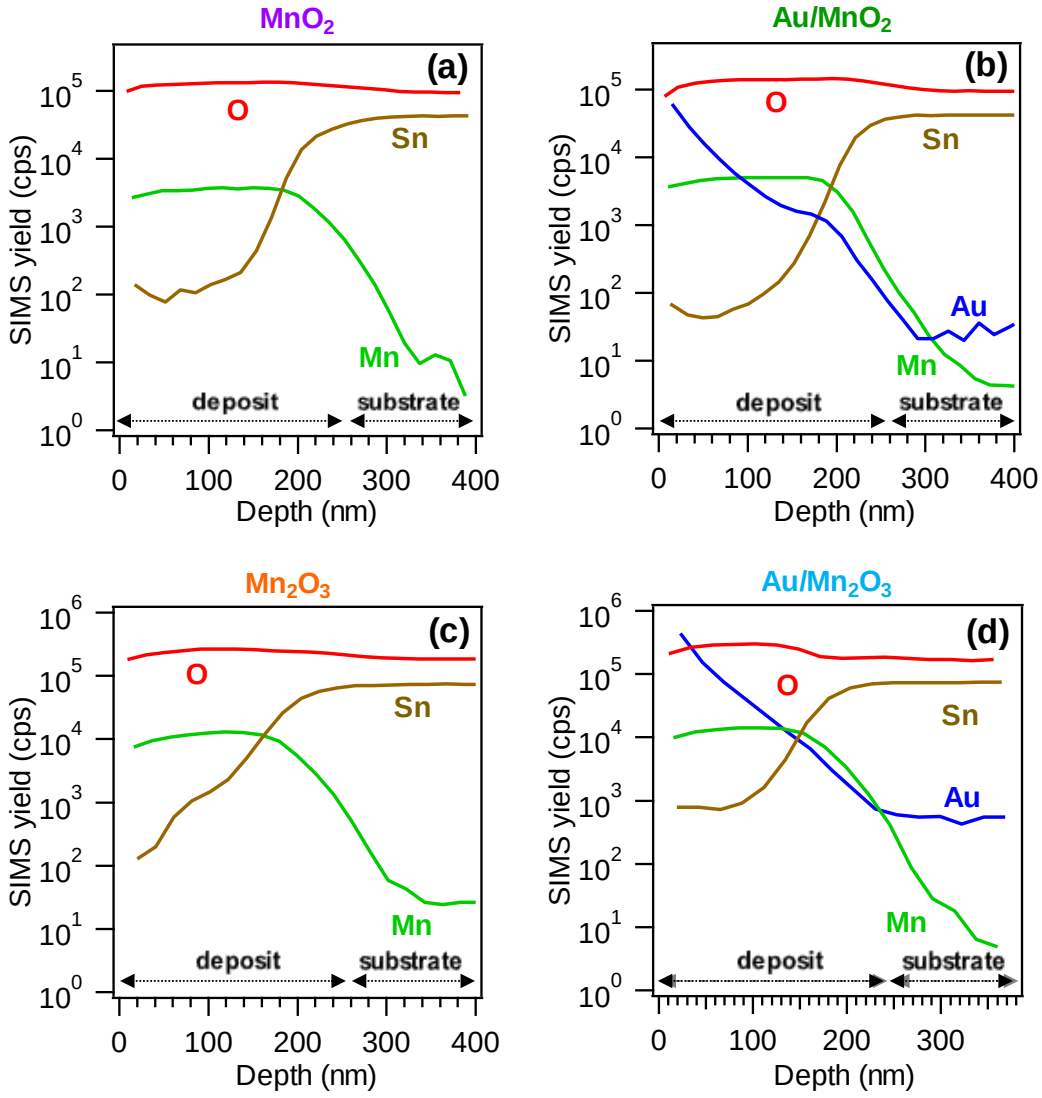

Figure 3. SIMS depth profiles of bare and gold-decorated Mn_xO_y (MnO_2, Mn_2O_3) samples.

Secondary ion mass spectrometry (SIMS) analyses were subsequently undertaken to probe the system in-depth composition and obtain complementary information with respect to XPS ones. Irrespective of preparative conditions, SIMS profiles (Figure 3) clearly revealed a nearly parallel trend for manganese and oxygen yields from the surface down to the deposit/substrate interface, in line with the uniform formation of single-phase MnO_2 or Mn_2O_3 throughout the deposit thickness. The relatively slow rise of tin signal was mainly related to the appreciable FTO roughness, as also evidenced by field emission-scanning electron microscopy (FE-SEM) and transmission electron microscopy (TEM) micrographs (see below). Interestingly, at

variance with Mn and O trends, the Au ionic yield progressively decreased within the deposit indicating that, despite gold was preferentially concentrated close to the Mn_xO_y surface, it was also dispersed in the inner *host* matrix regions. This result can be traced back to the synergy between the porous Mn_xO_y morphology and the inherent RF-sputtering infiltration power (see also Scheme 1).[33,34]

Optical absorption spectra of bare Mn_xO_y samples and gold-decorated ones are reported in Figure 4. All samples showed a progressively increasing absorption at lower wavelengths, that turned out to be steeper below 800 nm. in line with the occurrence of Mn_xO_y interband electronic transitions. Tauc plots analysis (see insets in Figures 4a and 4b) yielded band gap (E_G) values of ≈2.0 and ≈2.1 eV for MnO_2- and Mn_2O_3-based materials, respectively, in good agreement with previous literature data.[10,22,32] The absorption tail extending towards the near-infrared region was attributed to the presence of oxygen vacancies promoting the formation of sub-band gap states.[32,44] The sub-bandgap absorption tailing was present even for gold-free samples, suggesting an appreciable concentration of oxygen vacancies even in bare MnO_2 and Mn_2O_3. This effect can favorably influence the system electrocatalytic performances[7,13,45,46] (see also below).

In line with the above XPS results, showing an increased O defect content for Au-decorated samples, the spectra in Figure 4 revealed an enhanced light absorption for Au/MnO_2 and Au/Mn_2O_3 specimens in comparison to the homologous bare manganese oxides, and a slight E_G decrease of ≈0.1 eV upon gold sputtering.[39,45,46]

The system morphology and nanoscale structure were investigated through the combined use of FE- SEM, atomic force microscopy (AFM) and TEM analyses. An overview of plane-view and cross-sectional morphology for all samples is given in Figure S2, Supporting Information. Irrespective of preparative conditions, specimens were formed by elongated lamellar structures (width ≈20-30 nm) whose interconnection produced a porous deposit [average thickness = (250±40) nm]. For Au/MnO_2 and Au/Mn_2O_3 samples, Mn_xO_y surface was

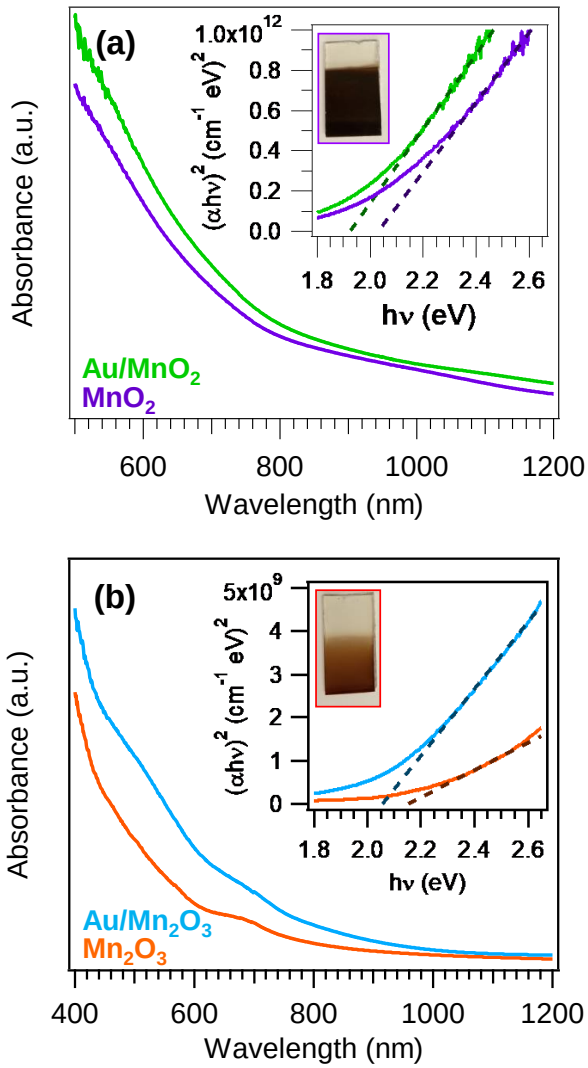

Figure 4. Optical absorption spectra of Mn_xO_y-based samples annealed in air (a) and Ar (b). The corresponding Tauc plots are given as insets, along with two digital micrographs of FTO-supported MnO_2 and Mn_2O_3 deposits. Compared to MnO_2, the paler Mn_2O_3 color is in line with the different ordinate range values revealed by Tauc plots.

uniformly decorated by small-sized gold NPs (see insets in plane-view images), whose formation was deemed to take place according to a three-dimensional (3D) Volmer-Weber growth mechanism.

Since roughness is also a determining factor influencing the ultimate electrocatalytic performances (a higher roughness typically corresponding to a higher active area),[18,32,33] the surface topography of the target systems was investigated by AFM. In this regard, micrographs in Figure S3, Supporting Information revealed a similar surface texture for all specimens and

yielded root-mean-square (RMS) roughness values of 25 ± 2 nm.

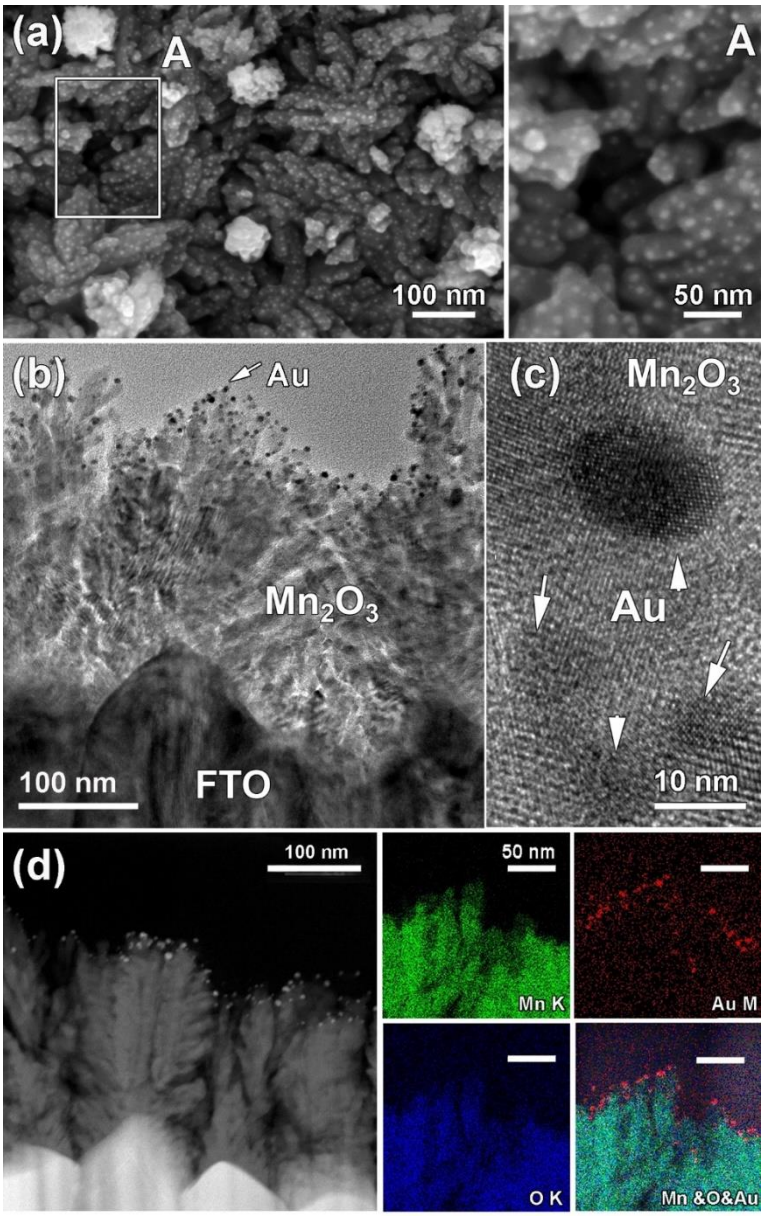

Figure 5. (a) Plane-view SEM micrograph of a Mn_2O_3 specimen functionalized with Au nanoparticles. The region marked by the white rectangle is displayed as an enlargement in panel A. (b) Low magnification cross-sectional bright field-TEM image of the same specimen. (c) High resolution-TEM (HR-TEM) image of selected Au nanoparticles deposited on Mn_2O_3. In panels (b) and (c), the dark contrast Au nanoparticles are marked by white arrows. (d) Cross-sectional high angle annular dark field-scanning TEM (HAADF-STEM) image and corresponding energy dispersive X-ray spectroscopy (EDXS) mapping of Mn K (green), Au M (red), and O K (blue) lines. An overlayed map superimposing manganese, gold and oxygen X-ray signals is presented in the bottom right corner panel.

Subsequently, special attention was devoted to the thorough analysis of gold-containing samples by TEM and EDXS. To this aim, Figures 5b-d provide a detailed insight into the structural and compositional features of the Au/Mn_2O_3 sample (see Figure 5a). Figure 5b displays a representative cross-sectional bright field TEM micrograph, which evidenced the formation of dendritic branched structures. The latter were found to outgrow from the zig-zag shape faceted surface of the underlying FTO substrate, giving rise to irregular nanodeposits with an open morphology. The typical lateral size of manganese oxide dendrites was 100-150 nm (Figures 5b and d). Such nanostructures, whose formation takes place at higher growth rates under a diffusion-controlled kinetic regime,[47-49] are highly desirable for the target applications thanks to the low branch radial size and high material/electrolyte contact area, which, in turn, reduce charge carrier diffusion distances and favorably affect interfacial reactions.[50] Indeed, the numerous lateral trunk/branch junctions provide a direct pathway for carrier collection from the various terminals to the central trunk.[47] Furthermore, the very open dendritic structure favors the efficient dispersion of gold NPs into the manganese oxide *host* matrix. In this regard, Figure 5b clearly reveals that Mn_2O_3 nanostructures were evenly decorated by tiny Au nanograins, which could be evidently discerned due the image contrast enabled by the large difference in manganese and gold atomic numbers (Z = 25 and 79, respectively). The average size of gold nanoaggregates was estimated to be ≈10 nm (Figure 5c), consistently with SEM data. Their high dispersion, relatively low amount and small size account for the lack of detectable Au reflections in the recorded XRD patterns (see above and Figure 1). Nonetheless, Figure 5c also clearly reveals a very intimate *host-guest* contact, with gold NPs embedded into the manganese oxide *hosts*. These findings are in line with the occurrence of a SMSI,[26,27,29-31] whose influence on the material electrochemical performances will be discussed later.

Additional important information could be gained by the combined use of HAADF-STEM imaging and simultaneous EDXS chemical mapping (Figure 5d). These analyses revealed that gold nanoparticles were predominantly located in the near-surface regions of manganese oxide

dendrites, following the landscape of Mn_2O_3 "trees". Nevertheless, a careful image inspection enabled to observe a certain in-depth Au dispersion throughout the entire structure, in accordance with SIMS results (see above and Figure 3).

In the case of MnO_2-based specimens, TEM analyses yielded qualitatively similar characteristics concerning both the deposit structure and the spatial distribution of Au particles (see Figure S4, Supporting Information). The morphological features of the obtained materials and the intimate contact between gold aggregates and the underlying manganese oxides is indeed an important issue to profitably exploit their mutual electronic and chemical interplay, ultimately yielding an appreciable performance enhancement in comparison to bare Mn_xO_y.

The OER performances of the developed FTO-supported electrocatalysts were preliminarily investigated in 0.5 M KOH aqueous solutions. Figure 6a displays the linear sweep voltammetry (LSV) curves for bare and gold-decorated Mn_xO_y (MnO_2, Mn_2O_3) samples. As a general rule, current density (j) values increased with the applied potential (E_{WE}), indicating a progressively more effective water oxidation at the electrode surface. Interestingly, catalytic activity systematically increased in the order MnO_2 < Au/MnO_2 <<< Mn_2O_3 < Au/Mn_2O_3, indicating that: i) Mn_2O_3 was much more active than MnO_2; ii) for both Mn_xO_y polymorphs, the introduction of gold NPs enhanced OER performances. Concerning issue i), it is worth recalling that MnO_2 and Mn_2O_3 matrices were prepared starting from the same Mn-O deposit (see Scheme 1) and, after thermal treatment, presented similar morphological features. Hence, since the two samples only differed in their crystal structure and related surface chemistry [*i.e.* Mn(IV) *vs*. Mn(III)], the present findings highlight the superior catalytic activity of β-Mn_2O_3 (*bixbyite*) compared to β-MnO_2 (*pyrolusite*) under the adopted experimental conditions, a topic that has been a matter of debate.[9,18,24]

The current density enhancement occurring upon Mn_xO_y decoration with gold NPs can be mainly traced back to local interfacial effects between Au and Mn_xO_y. In this regard, consistently with the above XPS data, some authors have reported that gold NPs, even in trace

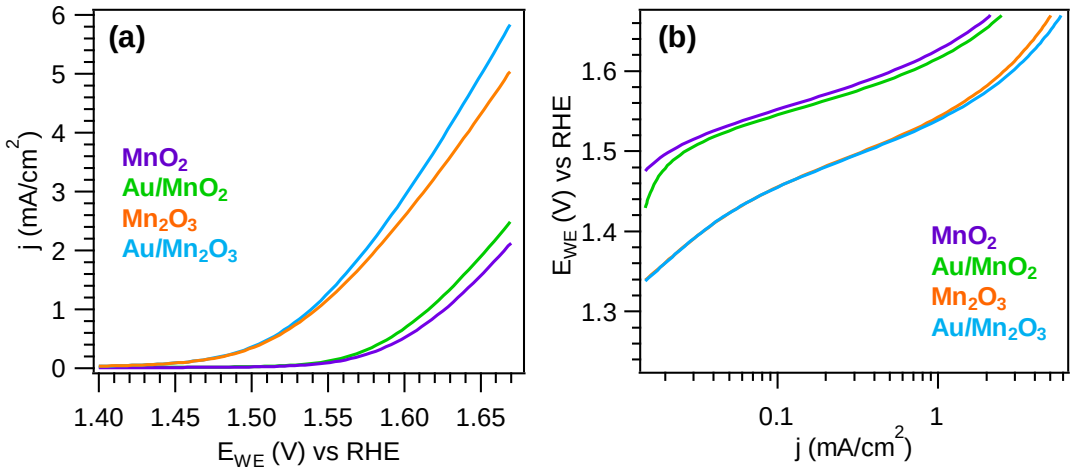

	j @ 1.65 V vs. RHE (mA/cm^2)	η @ 1 mA/cm^2 (mV)	Tafel slope (mV/decade)
MnO_2	1.57	396	66
Au/MnO_2	1.90	386	64
Mn_2O_3	4.31	312	84
Au/Mn_2O_3	4.97	309	82

Figure 6. (a) Current density *vs.* potential curves and (b) Tafel plots for Mn_xO_y-based samples. Current densities (j) at 1.65 V, overpotentials (η) at 1 mA/cm^2, and Tafel slope values are reported for each of the target specimens.

amounts, can donate electron density to neighboring Mn sites at the interface with Au NPs.[2,21,39] The latter phenomenon is also likely accompanied by the formation of oxygen vacancies close to the Au/Mn_xO_y interface, in line with XPS results and optical absorption spectra.[7,25,30,43,45] Hence, the improved OER performances of gold-containing samples with respect to bare Mn_xO_y specimens can be related to the higher content of oxygen vacancies, whose presence favorably impacts on adsorption, activation and dissociation steps.[32,34,35,37,40,42,46] Based on the above hypothesis, in good agreement with the occurrence of a SMSI effect,[26,28-31,39,43] the main role of gold NPs is to locally activate the *host* Mn_xO_y matrices, rendering them more effective OER catalysts.[2] Nevertheless, it is worth recalling that the higher oxygen vacancies content in Au/MnO_2 and Au/Mn_2O_3 might partially be due to a preferential oxygen removal during the sputtering step (see Scheme 1).[29,35]

Overall, j values up to ≈5 mA/cm^2 at 1.65 V *vs*. the reversible hydrogen electrode (RHE) were obtained (see table in Figure 6). Such results are similar or even better than other Mn_xO_y-based materials reported in the literature,[1,2,5,9,18,19,23] candidating the present systems as appealing OER electrocatalysts. In line with the above described current density trend for the various specimens, overpotentials (η) at 1 mA/cm^2 decreased following the opposite order, *i.e.*: MnO_2 > Au/MnO_2 > Mn_2O_3 > Au/Mn_2O_3 (see Figure 6). However, the analysis of Tafel plots in Figure 6b revealed a more complex dependence on the system composition. In fact, gold-decorated samples exhibited Tafel slope values lower than the corresponding bare Mn_xO_y specimens, indicating a beneficial role of Au NPs on OER kinetics.[1,2,21,28] Yet, if MnO_2-based samples are compared with Mn_2O_3-based ones, the latter were characterized by higher values. This result, apparently in contrast with the corresponding current density and overpotential value trends, can be explained taking into account: i) a different rate determining step and/or reaction mechanism[51] for the two manganese oxide polymorphs (the Tafel slope decreases once the rate-determining step is closer to the end step of a series of reactions);[52] ii) a higher surface coverage of MnO_2-based materials by reaction intermediates (the higher the coverage, the lower the Tafel slope value).[53] A predominance of the latter effect can indeed account for the lower catalytic activity of MnO_2-based samples compared to Mn_2O_3-based ones.

3. Conclusions

In the present work, we have proposed an original, versatile and potentially scalable route for the fabrication of Mn oxide-based electrocatalysts and for the enhancement of their OER performances. Characterization results revealed indeed the possibility to achieve the selective formation of the desired Mn_xO_y (MnO_2, Mn_2O_3) polymorph featuring an open dendritic morphology and a high content of oxygen vacancies. In addition, the eventual decoration of the obtained Mn_xO_y *host* matrices by highly dispersed *guest* Au NPs promoted the occurrence of a SMSI effect at the Au/Mn_xO_y interface. Tailoring of manganese oxide phase composition, along

with the amount of oxygen vacancies and the introduction of gold species, allowed to tailor and improve material activity towards OER. Specifically, Mn_2O_3-based systems yielded current density values nearly 3 times higher than the corresponding MnO_2-based ones, highlighting thus the better performances of manganese(III) oxide systems under the adopted conditions. Gold introduction induced a ≈20% improvement, despite its very small amount, due to the above mentioned SMSI. In this regard, it is worth noticing that, although the SMSI effect has been traditionally reported for hydrogen-involving reactions, its beneficial role has recently been reported under oxidative conditions,[26,27,31] and hence represent an "old tool for new applications", whose potential should still be fully exploited for OER catalysis. Overall, the obtained results can act as a pointer for the improvement of OER performances of transition metal oxide nanomaterials fabricated by means of controllable strategies. In perspective, the presently reported data can yield a valuable contribution in the fields of commercially viable water electrolysis for the sustainable production of hydrogen fuel, eventually even by (photo)electrochemical processes.

4. Experimental Section

Synthesis: The target materials were grown using a custom-built plasmochemical reactor consisting of a metal vacuum chamber equipped with two vertical electrodes. Pre-cleaned[54] FTO-coated glass slides (Aldrich®; ≈7 $\Omega \times sq^{-1}$; FTO layer thickness ≈600 nm), were fixed on the grounded electrode, whose temperature was measured by a thermocouple inserted into the resistively heated sample holder, whereas Radio Frequency (RF)-power (13.56 MHz) was delivered to a second electrode. In the PA-CVD of manganese oxides, electronic grade Ar and O_2 were used as plasma sources. The molecular precursor, $Mn(hfa)_2TMEDA$ (Hhfa = 1,1,1,5,5,5-hexafluoro-2,4-pentanedione; TMEDA = *N*,*N*,*N'*,*N'*-tetramethylethylenediamine),[37] was placed in a glass reservoir maintained at 70°C, and

introduced into the reactor by an Ar flow [60 standard cubic centimeters per minute (sccm)] through gas lines heated at 130°C in order to prevent undesired condensation phenomena. Two additional independent inlets were used for the introduction into the reactor of O_2 (5 sccm) and Ar (15 sccm). After a preliminary optimization, PA-CVD processes were carried out for 60 min using a RF-power of 20 W and a deposition temperature of 300°C, at a total pressure of 1.0 mbar.

Subsequently, functionalization with gold nanoparticles was performed by RF-sputtering from Ar plasmas using the same instrumentation. The obtained manganese oxides were used as substrates and mounted on the grounded electrode, whereas a gold target (BALTEC AG, 99.99%) was fixed on the RF one. RF-sputtering was carried out under optimized conditions, that enabled to avoid a complete manganese oxide coverage by a continuous gold overlayer (growth temperature = 60°C, total pressure = 0.3 mbar, Ar flow rate = 10 sccm, RF-power = 5 W, sputtering time = 30 min).

Finally, *ex-situ* thermal treatment was performed at 500°C for 60 min, under Ar or air to direct the system evolution towards the formation of Mn_2O_3- or MnO_2-based electrodes,[18] respectively.

Characterization: XRD patterns were collected with a Bruker D8 Advance diffractometer equipped with a Göbel mirror, using a CuKα X-ray source operated at 40 kV and 40 mA. The patterns were acquired in the 16-52° 2θ range (0.03°×step^{-1} and 10 s×step^{-1}).

XPS analyses were performed by a Perkin-Elmer Φ 5600-ci spectrometer using a standard Al Kα radiation (1486.6 eV). The sample analysis area was 800 μm in diameter. Due to the Mn3s and Au4f photoelectron peak overlap, quantitative analysis was based on the interference-free Au4$d_{5/2}$ signal.[55] BE values (uncertainty = ±0.2 eV) were corrected for charging by assigning to the adventitious C1s peak a BE value of 284.8 eV. Data analysis involved Shirley-type background subtraction and peak area determination by integration, eventually using non-

linear least-squares curve fitting adopting Gaussian-Lorentzian peak shapes. Atomic compositions were evaluated from peak areas using sensitivity factors supplied by Perkin Elmer.

SIMS depth profiles were recorded by an IMS 4f mass spectrometer (Cameca), using a Cs^+ primary beam (voltage = 14.5 keV; current = 25 nA; stability = 0.3%). Rastering was performed over a 150×150 μm^2 nominal area, and negative secondary ions were collected from a 7×7 μm^2 sub-region in order to avoid crater effects. Charge compensation was performed by means of an electron gun. The analyses were carried out in high mass resolution configuration, to avoid mass interference artifacts, and beam blanking mode, to improve the depth resolution. The sputtering time in the profile abscissa was converted into depth values basing on the deposit thickness measured by FE-SEM analyses (see below).

Optical absorption spectra were registered by means of a Cary 50 (Varian) dual-beam spectrophotometer (spectral bandwidth = 1 nm), operating in transmission mode and at normal incidence. In each spectrum, the FTO substrate contribution was subtracted. Extrapolation of band gap values was performed using the Tauc equation $(\alpha h\nu)^2$ *vs*. $h\nu$, where α is the absorption coefficient, assuming direct and allowed transitions for both MnO_2- and Mn_2O_3-based systems.[10,22,32]

Plane-view and cross-sectional FE-SEM images were collected out by means of a Zeiss SUPRA 40VP microscope, operating at primary beam acceleration voltages of 10 kV and collecting electrons by means of an in-lens detector. The mean deposit thickness and particle dimensions were estimated using the ImageJ® software.[56]

AFM micrographs were recorded using an NT-MDT SPM Solver P47H-PRO apparatus, operating in semi-contact mode. All measurements were performed in air at room temperature. RMS roughness values were obtained from the height profiles of 3×3 μm^2 after background subtraction.

Thin cross-sectional samples for TEM characterization were prepared by the focused ion beam technique (FIB), using a Helios 450s FIB/SEM instrument (Thermo Fisher, USA). Pre-thinned lamellas were lifted out from the target material, attached to a TEM grid and subsequently thinned up to electron transparency. Final cleaning was performed by FIB, operating at 5 kV and low current (25 pA). During sample preparation, when necessary, a Pt protective layer was deposited over the structures to embed them and prevent them from collapsing. HR-TEM, HAADF-STEM, and EDXS analyses of Mn_2O_3-based specimens were performed using an aberration double-corrected cold FEG JEM ARM200F apparatus operated at 200 kV, equipped with a CENTURIO EDXS detector, ORIUS Gatan camera and Quantum GIF. Analyses on MnO_2-based specimens were carried out by an aberration corrected FEI Titan^3 60-300 kV microscope operated at 300 kV.

Electrochemical tests: The electrochemical performances of the target systems towards OER were assessed using a three-electrode set-up, using a VMP3 (BioLogic Science Instruments) working station. A Pt mesh, a Hg/HgO (MMO) electrode and the target FTO-supported materials were used as the counter, reference and working electrode, respectively. The potential was transformed into the RHE scale using the relation:[9]

$$E_{RHE}(V) = E_{MMO}(V) + 0.0592 \times pH + 0.111 \quad (1)$$

The presented electrochemical data do not include compensation for the series resistance of the solution. LSV curves were registered in freshly prepared 0.5 M KOH solutions at a scan rate of 1 $mV \times s^{-1}$, and the measured currents were normalized to the electrode geometric area (geometric area ≈1.0 cm^2). The OER overpotential (η) at 1 mA/cm^2 was calculated as:[11,20,23]

$$\eta\ (V) = E_{WE}\ (V\ vs.\ RHE) - 1.23 \quad (2)$$

where E_{WE} and 1.23 are the measured potential value and the standard potential of O_2 evolution *vs.* RHE, respectively. Tafel slopes were obtained by plotting E_{WE} *vs.* the current density logarithm.[4,18-20,57]

Supporting Information
Supporting Information is available from the Wiley Online Library or from the author.

Acknowledgements

Padova University (DOR 2017–2019 and P-DiSC #03BIRD2018-UNIPD OXYGENA projects), as well as the INSTM Consortium (INSTMPD004 – NETTUNO project) and AMGA Foundation (Mn4Energy project), are gratefully acknowledged for financial support. The Qu-Ant-EM microscope was partly funded by the Hercules fund from the Flemish Government. J.V. acknowledges funding from a GOA project 'Solarpaint' from the University of Antwerp and from EU H2020 823717 ESTEEM3 project. The authors thank Dr. Daniele Valbusa, Dr. Gianluca Corrò, Dr. Andrea Gallo and Dr. Dileep Khrishnan for helpful experimental assistance.

Received: ((will be filled in by the editorial staff))
Revised: ((will be filled in by the editorial staff))
Published online: ((will be filled in by the editorial staff))

References

[1] R. Frydendal, L. C. Seitz, D. Sokaras, T. C. Weng, D. Nordlund, I. Chorkendorff, I. E. L. Stephens, T. F. Jaramillo, *Electrochim. Acta* **2017**, *230*, 22.

[2] Y. Gorlin, C.-J. Chung, J. D. Benck, D. Nordlund, L. Seitz, T.-C. Weng, D. Sokaras, B. M. Clemens, T. F. Jaramillo, *J. Am. Chem. Soc.* **2014**, *136*, 4920.

[3] Z. S. Luo, E. Irtem, M. Ibanez, R. Nafria, S. Marti-Sanchez, A. Genc, M. de la Mata, Y. Liu, D. Cadavid, J. Llorca, J. Arbiol, T. Andreu, J. R. Morante, A. Cabot, *ACS Appl. Mater. Interfaces* **2016**, *8*, 17435.

[4] Y. T. Meng, W. Q. Song, H. Huang, Z. Ren, S. Y. Chen, S. L. Suib, *J. Am. Chem. Soc.* **2014**, *136*, 11452.

[5] S. Hernandez, C. Ottone, S. Varetti, M. Fontana, D. Pugliese, G. Saracco, B. Bonelli, M. Armandi, *Materials* **2016**, *9*, 296.

[6] Y. Gorlin, B. Lassalle-Kaiser, J. D. Benck, S. Gul, S. M. Webb, V. K. Yachandra, J. Yano, T. F. Jaramillo, *J. Am. Chem. Soc.* **2013**, *135*, 8525.

[7] Y. Zhao, C. Chang, F. Teng, Y. Zhao, G. Chen, R. Shi, G. I. N. Waterhouse, W. Huang, T. Zhang, *Adv. Energy Mater.* **2017**, *7*, 1700005.

[8] R. Frydendal, M. Busch, N. B. Halck, E. A. Paoli, P. Krtil, I. Chorkendorff, J. Rossmeisl, *ChemCatChem* **2015**, *7*, 149.

[9] S. Lian, M. P. Browne, C. Domínguez, S. N. Stamatin, H. Nolan, G. S. Duesberg, M. E. G. Lyons, E. Fonda, P. E. Colavita, *Sustainable Energy Fuels* **2017**, *1*, 780.

[10] B. A. Pinaud, Z. B. Chen, D. N. Abram, T. F. Jaramillo, *J. Phys. Chem. C* **2011**, *115*, 11830.

[11] P.-P. Liu, T.-T. Li, H.-L. Zhu, Y.-Q. Zheng, *J. Solid State Electrochem.* **2018**, *22*, 2999.

[12] M. Fekete, R. K. Hocking, S. L. Y. Chang, C. Italiano, A. F. Patti, F. Arena, L. Spiccia, *Energy Environ. Sci.* **2013**, *6*, 2222.

[13] H. Antoni, W. Xia, J. Masa, W. Schuhmann, M. Muhler, *Phys. Chem. Chem. Phys.* **2017**, *19*, 18434.

[14] F. Urbain, R. Du, P. Tang, V. Smirnov, T. Andreu, F. Finger, N. Jimenez Divins, J. Llorca, J. Arbiol, A. Cabot, J. R. Morante, *Appl. Catal., B* **2019**, *259*, 118055.

[15] K. L. Pickrahn, S. W. Park, Y. Gorlin, H.-B.-R. Lee, T. F. Jaramillo, S. F. Bent, *Adv. Energy Mater.* **2012**, *2*, 1269.

[16] Z. N. Zahran, E. A. Mohamed, Y. Naruta, *ACS Catal.* **2016**, *6*, 4470.

[17] I. G. McKendry, L. J. Mohamad, A. C. Thenuwara, T. Marshall, E. Borguet, D. R. Strongin, M. J. Zdilla, *ACS Energy Lett.* **2018**, *3*, 2280.

[18] F. Mattelaer, T. Bosserez, J. Ronge, J. A. Martens, J. Dendooven, C. Detavernier, *RSC Adv.* **2016**, *6*, 98337.

[19] H. Sim, J. Lee, T. Yu, B. Lim, *Korean J. Chem. Eng.* **2018**, *35*, 257.

[20] M. Tahir, L. Pan, F. Idrees, X. Zhang, L. Wang, J.-J. Zou, Z. L. Wang, *Nano Energy* **2017**, *37*, 136.

[21] C.-H. Kuo, W. Li, L. Pahalagedara, A. M. El-Sawy, D. Kriz, N. Genz, C. Guild, T. Ressler, S. L. Suib, J. He, *Angew. Chem. Int. Ed.* **2015**, *54*, 2345.

[22] R. Naeem, M. A. Ehsan, R. Yahya, M. Sohail, H. Khaledi, M. Mazhar, *Dalton Trans.* **2016**, *45*, 14928.

[23] A. Ramírez, P. Hillebrand, D. Stellmach, M. M. May, P. Bogdanoff, S. Fiechter, *J. Phys. Chem. C* **2014**, *118*, 14073.

[24] R. Pokhrel, M. K. Goetz, S. E. Shaner, X. Wu, S. S. Stahl, *J. Am. Chem. Soc.* **2015**, *137*, 8384.

[25] F. Cheng, T. Zhang, Y. Zhang, J. Du, X. Han, J. Chen, *Angew. Chem. Int. Ed.* **2013**, *52*, 2474.

[26] K. Fujiwara, K. Okuyama, S. E. Pratsinis, *Environ. Sci.: Nano* **2017**, *4*, 2076.

[27] Y. Zhou, C. Jin, Y. Li, W. Shen, *Nano Today* **2018**, *20*, 101.

[28] A. Longo, L. F. Liotta, G. D. Carlo, F. Giannici, A. M. Venezia, A. Martorana, *Chem. Mater.* **2010**, *22*, 3952.

[29] C.-J. Pan, M.-C. Tsai, W.-N. Su, J. Rick, N. G. Akalework, A. K. Agegnehu, S.-Y. Cheng, B.-J. Hwang, *J. Taiwan Inst. Chem. Eng.* **2017**, *74*, 154.

[30] I. Ro, J. Resasco, P. Christopher, *ACS Catal.* **2018**, *8*, 7368.

[31] H. He, J. Chen, D. Zhang, F. Li, X. Chen, Y. Chen, L. Bian, Q. Wang, P. Duan, Z. Wen, X. Lv, *ACS Catal.* **2018**, *8*, 6617.

[32] D. Barreca, F. Gri, A. Gasparotto, G. Carraro, L. Bigiani, T. Altantzis, B. Žener, U. Lavrenčič Štangar, B. Alessi, D. B. Padmanaban, D. Mariotti, C. Maccato, *Nanoscale* **2019**, *11*, 98.

[33] L. Bigiani, D. Zappa, E. Comini, C. Maccato, A. Gasparotto, D. Barreca, *J. Nanosci. Nanotechnol.* **2020**, *20*, 3025.

[34] L. Bigiani, D. Zappa, C. Maccato, E. Comini, D. Barreca, A. Gasparotto, *Appl. Surf. Sci.* **2020**, *512*, 145667.

[35] W. Li, S. Liu, S. Wang, Q. Guo, J. Guo, *J. Phys. Chem. C* **2014**, *118*, 2469.

[36] Pattern N° 024-0735, JCPDS (2000).

[37] D. Barreca, G. Carraro, E. Fois, A. Gasparotto, F. Gri, R. Seraglia, M. Wilken, A. Venzo, A. Devi, G. Tabacchi, C. Maccato, *J. Phys. Chem. C* **2018**, *122*, 1367.

[38] Pattern N° 041-1442, JCPDS (2000)

[39] L. Bigiani, T. Andreu, C. Maccato, E. Fois, A. Gasparotto, C. Sada, G. Tabacchi, D. Krishnan, J. Verbeeck, J. R. Morante, D. Barreca, *J. Mater. Chem. A* **2020**, 10.1039/D0TA05972B.

[40] L. Chen, J. Huang, R. Zeng, Y. Xiong, J. Wei, K. Yuan, Y. Chen, *Adv. Mater. Interfaces* **2020**, *7*, 1901729.

[41] http://srdata.nist.gov/xps.

[42] I. M. Nadeem, G. T. Harrison, A. Wilson, C. L. Pang, J. Zegenhagen, G. Thornton, *J. Phys. Chem. B* **2018**, *122*, 834.

[43] H. Wu, L. F. Liotta, in *Heterogeneous Gold Catalysts and Catalysis*, The Royal Society of Chemistry, 2014, 462.

[44] S. Jaiswar, K. D. Mandal, *J. Phys. Chem. C* **2017**, *121*, 19586.

[45] L. Li, X. H. Feng, Y. Nie, S. G. Chen, F. Shi, K. Xiong, W. Ding, X. Q. Qi, J. S. Hu, Z. D. Wei, L. J. Wan, M. R. Xia, *ACS Catal.* **2015**, *5*, 4825.

[46] J. A. Dawson, H. Chen, I. Tanaka, *ACS Appl. Mater. Interfaces* **2015**, *7*, 1726.

[47] M. J. Bierman, S. Jin, *Energy Environ. Sci.* **2009**, *2*, 1050.

[48] H. Brune, C. Romainczyk, H. Röder, K. Kern, *Nature* **1994**, *369*, 469.

[49] M. Cao, T. Liu, S. Gao, G. Sun, X. Wu, C. Hu, Z. L. Wang, *Angew. Chem. Int. Ed.* **2005**, *44*, 4197.

[50] G.-F. Li, M. Divinagracia, M. F. Labata, J. D. Ocon, P.-Y. Abel Chuang, *ACS Appl. Mater. Interfaces* **2019**, *11*, 33748.

[51] S. E. Balaghi, C. A. Triana, G. R. Patzke, *ACS Catal.* **2020**, *10*, 2074.

[52] N.-T. Suen, S.-F. Hung, Q. Quan, N. Zhang, Y.-J. Xu, H. M. Chen, *Chem. Soc. Rev.* **2017**, *46*, 337.

[53] T. Shinagawa, A. T. Garcia-Esparza, K. Takanabe, *Sci. Rep.* **2015**, *5*, 13801.

[54] D. Barreca, G. Carraro, A. Gasparotto, C. Maccato, C. Sada, A. P. Singh, S. Mathur, A. Mettenborger, E. Bontempi, L. E. Depero, *Int. J. Hydrogen Energy* **2013**, *38*, 14189.

[55] L. Bigiani, D. Barreca, A. Gasparotto, C. Maccato, *Surf. Sci. Spectra* **2018**, *25*, 014003.

[56] https://imagej.nih.gov/ij/.

[57] M. Huynh, D. K. Bediako, Y. Liu, D. G. Nocera, *J. Phys. Chem. C* **2014**, *118*, 17142.

Manganese oxide nanostructures functionalized with Au nanoparticles fabricated by a two-step plasma-assisted route pave the way to applications as improved anode catalysts for oxygen evolution in water splitting processes.

Keywords: manganese oxides; strong metal–support interaction; plasma assisted-chemical vapor deposition; sputtering; oxygen evolution reaction

Lorenzo Bigiani, Alberto Gasparotto, Teresa Andreu, Johan Verbeeck,*
Cinzia Sada, Evgeny Modin, Oleg I. Lebedev,
Juan Ramón Morante, Davide Barreca, and Chiara Maccato*

Au-manganese oxide nanostructures by a plasma-assisted process as electrocatalysts for oxygen evolution: a chemico-physical investigation